Typeset with jjap2.cls <ver.1.0> **Regular Paper**

Phase-resolved profiles of electron energy deposition in inductively coupled radio-frequency plasmas driven under confronting divergent magnetic fields *

Katsuhiro NAKASHIMA, Hironori TAKAHASHI and Hirotake SUGAWARA †

Graduate School of Information Science and Technology, Hokkaido University, Sapporo 060-0814, Japan

Electron motion in a cylindrical chamber under RF electric field and confronting divergent magnetic fields was simulated to evaluate the phase-resolved profiles of power deposition to electrons in a low-pressure inductively coupled magnetized plasma. There were three primary regions where the power deposition was high; a region near the RF antenna, a region near the sidewall, and a region of the partial resonance. The phase-resolved profiles of the electron energy gain $G(t)$ and azimuthal electron velocity $v_\theta(t)$ were obtained in every section defined in the chamber, and were fitted by functions with sinusoidal terms. The characteristics of $G(t)$ and $v_\theta(t)$, e.g. their asymmetry and directionality, particular to the position were discussed by comparisons between different regions with the fitting parameters and their factors, such as the amplitude of electric field, that of the azimuthal velocity, the power factor, and the phase differences from the RF electric field.

1. Introduction

Magnetic fields are often applied to plasmas for a certain effect on charged particles in the plasmas. For example, plasma confinement is utilized in fusion plasmas to keep them at a high density and away from the reactor walls, and magnetic filters are used to select specific species or to remove particles in plasma flow by its charge-to-mass ratio.[1–8] Recently, it was proposed to use the separatrix of confronting divergent magnetic fields (CDMFs, see Fig. 1) as a magnetic shutter[9] for an inductively coupled plasma (ICP). It is expected that plasma flow can be controlled by adjusting the aperture of the shutter via the coil currents inducing the magnetic fields. This technique would lead to a new way of plasma modulation and downsizing of remote plasmas. On the other hand, magnetic fields have simultaneously a cooling effect on electrons in plasmas.[10–16] The electron acceleration under electric fields is deterred by capture due to the electron cyclotron motion around magnetic flux lines. In order to sustain and control the magnetized plasmas stably, it is necessary to understand the mechanisms of power deposition to electrons under electric and magnetic fields.

*Published source: Japanese Journal of Applied Physics, Vol. 58, No. 11, 116001-1–116001-7 (2019), DOI: 10.7567/1347-4065/ab4481

†E-mail: sugawara@ist.hokudai.ac.jp

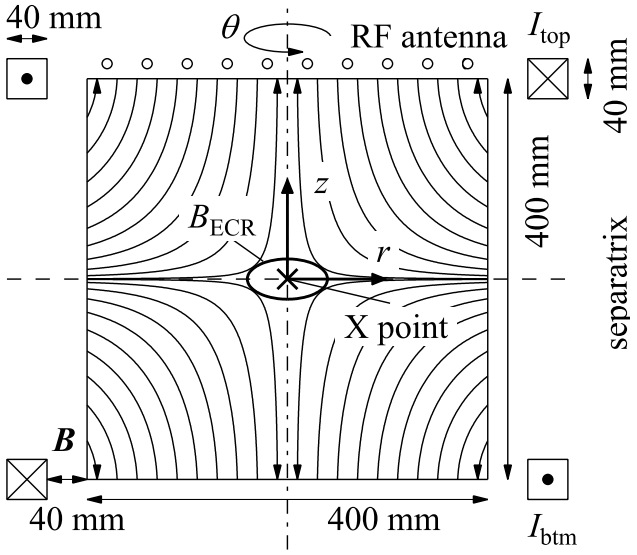

Fig. 1. Schematic of a model reactor and applied CDMFs. The CDMFs were applied by $I_{\rm top} = +I_{\rm dc}$ and $I_{\rm btm} = -I_{\rm dc}$, where $I_{\rm top} = +50.0\,\mathrm{A}$. The electric field was induced by an antenna current $+20\cos 2\pi f_{\rm RF} t\,\mathrm{A}$ at $f_{\rm RF} = 13.56\,\mathrm{MHz}$. A magnetic null point, named the X point, was formed at the center of the separatrix at $z = 0$.

The authors have analyzed fundamental structure and response of an ICP under the CDMFs, so-called the X-point plasmas developed as an ion source,[17–20] and it was reported that high energy deposition efficiency was observed in three characteristic regions.[21–24] The high efficiencies in the three regions were attributed to high electric fields under the RF antenna, the partial resonance[25,26] around the region of the RF-resonant magnetic field strength,[27] and a stochastic heating particular to the region near the sidewall.[24] The power deposition to electrons near the sidewall was indicated to occur in non-magnetized ICPs as well by high ionization rates and high number densities of excited particles observed there.[28–32] Some mechanisms of the power deposition to electrons such as anomalous skin effect in ICPs have also been investigated.[33–38] However, features of the power deposition specific to the three above-mentioned regions are still unclear from the viewpoint of microscopic electron motion because of the complexity of the electron behavior under non-uniform crossed electric and magnetic fields.

In this paper, the power deposition to electrons in an X-point plasma is analyzed using a Monte Carlo method. The time-resolved profiles of the electron energy gain (EEG) and the azimuthal electron velocity are sampled, and they are characterized using curve fitting parameters such as the amplitude of sinusoidal terms and phase difference from the RF electric field. Their position-dependent features are discussed for fundamental understanding of electron response in the CDMFs.

2. Simulation model and conditions

2.1 Reactor geometry

Figure 1 shows the reactor assumed in the present work. The reactor configuration is the same as that in previous work.[9,24,27] The chamber was a cylinder with a 40.0 cm inner diameter and a 40.0 cm height. The origin of position (x, y, z) in a Cartesian coordinate or (r, θ, z) in a cylindrical coordinate was defined at the center of the chamber. Here, r is the radial position satisfying $r^2 = x^2 + y^2$, z is the axial position, and θ is the azimuthal angle taken counterclockwise in the top view from the x-axis toward the y-axis as $x = r\cos\theta$ and $y = r\sin\theta$.

2.2 Electric and magnetic fields

It was assumed that the RF electric field $\boldsymbol{E}$ was induced by RF current

$$I_{\mathrm{antenna}}(t) = I_{\mathrm{RF}} \cos 2\pi f_{\mathrm{RF}} t \tag{1}$$

($f_{\mathrm{RF}} = 13.56\,\mathrm{MHz}$ and $I_{\mathrm{RF}} = +20\,\mathrm{A}$) flowing through a planar antenna on the chamber ceiling. $I_{\mathrm{antenna}}(t)$ was, for simplicity, assumed to flow concentric circular paths at $r = 2.0$, 6.0, 10.0, 14.0, and 18.0 cm and $z = 21.5\,\mathrm{cm}$ so that $\boldsymbol{E}$ had only the azimuthal component E_θ represented as

$$E_\theta(r, z, t) = -E_{\max}(r, z) \sin \omega_{\mathrm{RF}} t. \tag{2}$$

Here, $\omega_{\mathrm{RF}} = 2\pi f_{\mathrm{RF}}$, and the sign of E_θ was chosen so that the electron acceleration is toward the $+\theta$ direction in the former half of an RF period.

The CDMFs, $\boldsymbol{B}$, were applied by two 36-turn DC coaxial coils, the top and bottom coils, with a thickness of 4.0 cm × 4.0 cm, the inner and outer radii 24.0 and 28.0 cm, respectively, and the centers aligned at $z = Z_{\mathrm{top}} = +20.0\,\mathrm{cm}$ and $z = Z_{\mathrm{btm}} = -20.0\,\mathrm{cm}$ symmetrically. It was assumed that the same current I_{dc} was applied to the top and bottom coils in opposite directions as $I_{\mathrm{top}} = +I_{\mathrm{dc}}$ and $I_{\mathrm{btm}} = -I_{\mathrm{dc}}$, and $\boldsymbol{B}$ had only the radial and axial components, B_r and B_z, respectively. I_{dc} was set at +50 A. $\boldsymbol{B} = 0$ at the origin, and this magnetic null point is called the X point. $|\boldsymbol{B}|$ increases outward from the X point, and the X point is surrounded by a shell of $|\boldsymbol{B}| = B_{\mathrm{ECR}}$. Here, B_{ECR} is the RF-resonant magnetic field strength, near which high mean electron energy[39] and a high EEG[9,27] were observed, and $B_{\mathrm{ECR}} = 2\pi(m/e)f_{\mathrm{RF}} = 0.48\,\mathrm{mT}$ at $f_{\mathrm{RF}} = 13.56\,\mathrm{MHz}$. This phenomenon was mentioned as partial Larmor rotation[25] or partial resonance[26] in a similar magnetized plasma.

$B_r(r, z)$, $B_z(r, z)$, and $E_{\max}(r, z)$ were calculated on the basis of the Biot–Savart law and Faraday's law of induction, respectively, before the main simulation. Their r–z distributions were given to the main simulation program as maps of the $\boldsymbol{E}$ and $\boldsymbol{B}$ fields. Figure 2 shows the distributions of $E_{\max}$ and $|\boldsymbol{B}|$ in the rz-plane. The RF magnetic field induced by the RF $\boldsymbol{E}$ field was neglected because it was much smaller than the DC $\boldsymbol{B}$ field. Although the space

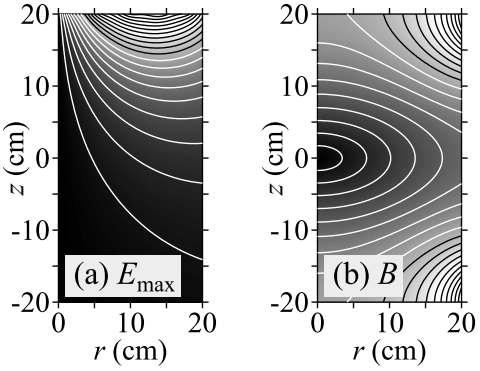

Fig. 2. Distributions of the electric and magnetic fields (a) $E_{\max}(r, z)$ and (b) $|\boldsymbol{B}(r, z)|$ relative to their maxima, from black for 0 to white for 1. The contours are in steps of 0.05; the whites for 0.05–0.45 and the blacks for 0.50–0.95.

charge field has been considered in some previous simulations of magnetized plasmas,[27,40] the present simulation assumed a condition free from the space charge field to focus exclusively on the effect of the directionality of electron flow originating from the arrangement of the crossed $\boldsymbol{E}$ and $\boldsymbol{B}$ fields and to be consistent with the preceding simulations of the X-point plasma.[9,24] Some related simulations indicate that the DC field of the sheath promotes the EEG, especially that by high-energy electrons, in a similar way to the electron reflection at the sidewall,[41–43] and that primary structures and dynamics of the X-point plasma remain even without the space charge field.[44]

2.3 Tracking of electrons

The initial electrons were supplied uniformly from the chamber ceiling with initial velocities chosen at random from a Maxwellian distribution with a mean energy of 1.0 eV. The number of initial electrons was 10^5. The electron trajectory was calculated by solving the following electron motion equations using the Runge–Kutta method:

$$\frac{d\boldsymbol{v}}{dt} = -\frac{e}{m}(\boldsymbol{E} + \boldsymbol{v} \times \boldsymbol{B}), \quad \frac{d\boldsymbol{r}}{dt} = \boldsymbol{v}, \tag{3}$$

where $\boldsymbol{r}$ and $\boldsymbol{v}$ are the position and velocity of an electron, and e and m are the electronic charge and mass, respectively. The simulation time step Δt was 3.7 ps, which is 1/20 000 of the RF period $T_{\mathrm{RF}} = 1/f_{\mathrm{RF}} = 73.7$ ns. This Δt value is sufficiently fine to draw an electron locus under cyclotron motion.

The gas was assumed to be Ar at 0.67 Pa at 300 K. Some additional pressures, 0.00, 0.13, and t0.40 Pa, were adopted in part for comparisons. The occurrence of the collisional events was judged by a time-saving scheme[45] using random numbers on the basis of the collision probability. The probability was derived from the electron collision cross sections for Ar taken from Ref. 46. The cross section set of Ar includes processes of elastic collision,

excitation, and ionization. A perfect elastic reflection was assumed at the chamber wall. The tracking time was $200T_{\mathrm{RF}}$. The sampling of the profiles of the electron motion was made during $150T_{\mathrm{RF}} \leq t \leq 200T_{\mathrm{RF}}$, until which the initial electrons diffused over the upper region of the chamber where the electrons were confined by the CDMFs.

3. Sampling

3.1 Sections for sampling

The chamber space (r, θ, z) was mapped onto two-dimensional space (r, z) under an assumption of rotational symmetry with respect to θ, and the (r, z) space was partitioned into sections for every Δr and Δz. The (i, j)th sampling section $S_{i,j}$ is defined as the region of $(i-1)\Delta r \leq r < i\Delta r$ and $(j-1)\Delta z + Z_{\mathrm{btm}} \leq z < j\Delta z + Z_{\mathrm{btm}}$. The resolution was set as $\Delta r = \Delta z = 0.5\,\mathrm{cm}$, thus $1 \leq i \leq 40$ and $1 \leq j \leq 80$.

3.2 Azimuthal electron velocity

The azimuthal electron velocity v_θ is a quantity convertible to the loop current in a macroscopic view, which is regarded as the secondary coil current to be magnetically coupled with the RF antenna current in a transformer equivalent circuit model.[47]

The azimuthal electron velocity $v_\theta(S_{i,j}, t)$ in $S_{i,j}$ was sampled as follows:

$$v_\theta(S_{i,j}, t) = \left(\sum_{S_{i,j} \ni \boldsymbol{r}_k} v_{\theta,k}(t)\right) / \left(\sum_{S_{i,j} \ni \boldsymbol{r}_k} 1\right), \tag{4}$$

$$v_{\theta,k}(t) = -v_{x,k}(t)\sin\theta_k(t) + v_{y,k}(t)\cos\theta_k(t), \tag{5}$$

where $v_{x,k}(t)$, $v_{y,k}(t)$, and $v_{\theta,k}(t)$ are the x, y, and azimuthal components of the velocity $\boldsymbol{v}_k(t)$ of the kth electron, respectively. The summation applies only to the electrons resident in $S_{i,j}$ at t. $v_\theta > 0$ represents electron flow towards the $+\theta$ direction, i.e. counterclockwise around the z-axis in the top view, and $v_\theta < 0$ for the clockwise towards the $-\theta$ direction (see Fig. 3).

The sampled $v_\theta(S_{i,j}, t)$ values were approximated by the following function by a fitting using the least squares method:

$$v_\theta(S_{i,j}, t) = v_1(S_{i,j})\sin[\omega_{\mathrm{RF}}t - \phi_1(S_{i,j})] + v_0(S_{i,j}). \tag{6}$$

Here, note that the fitting may have two solutions because $v_1\sin(\omega_{\mathrm{RF}}t - \phi_1) = -v_1\sin(\omega_{\mathrm{RF}}t - (\phi_1 + \pi))$. To make the fitting function unique, v_1 was taken to be positive, and its phase delay ϕ_1 is defined in a range of $-\pi \leq \phi_1 < \pi$. A positive ϕ_1 value represents a phase delay of $v_\theta(S_{i,j}, t)$ from $-E_\theta(t)$. This formula assumes that $v_\theta(S_{i,j}, t)$ alternates with $E_\theta(t)$, and its time-averaged value v_0 may be non-zero, i.e. the loop current at a specific position may be asymmetric between the former and latter halves of an RF period.

Such an asymmetry is seen indirectly in observation results of optical emission from a magnetized plasma.[48] It is known that the gradient of the $\boldsymbol{B}$ field induces the grad-B drift toward the direction of $-\boldsymbol{B} \times \nabla|\boldsymbol{B}|$. If collisionless, the grad-B drift would occur toward the

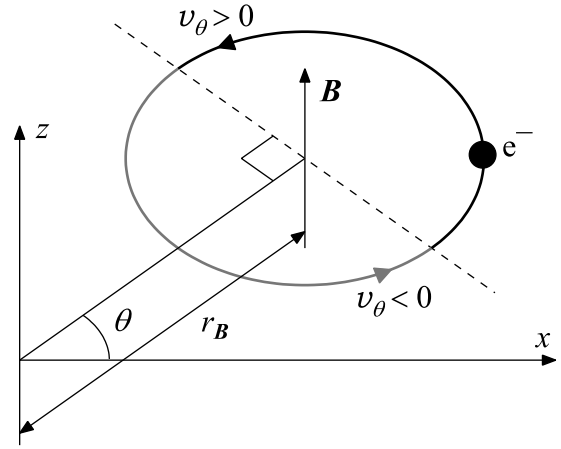

Fig. 3. Contribution of electron cyclotron motion to v_θ. The electron gyrating around the magnetic field line contributes to the azimuthal velocity component positively when $r > r_{\boldsymbol{B}}$ and negatively when $r < r_{\boldsymbol{B}}$.

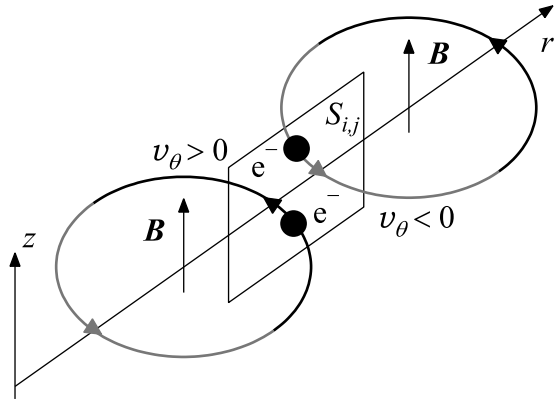

Fig. 4. Contribution of inside and outside electrons to v_θ sampled in a section $S_{i,j}$.

$+\theta$ direction in the upper region ($z > 0$) in the chamber under the present field configuration. Furthermore, it was pointed out that $v_\theta(S_{i,j}, t)$ may have a directionality because of the rectification effect originating from the arrangement of the crossed electric and magnetic fields.[49–51] The directionality of the electron drift was also observed in a simulation of electron motion in antiparallel gradient magnetic fields.[26,52,53] The directionality was explained on the basis of the electron cyclotron motion and the number density gradient of the spatial electron distribution.[21] Figure 4 shows that the contribution of an electron gyrating outside of $S_{i,j}$ to v_θ in $S_{i,j}$ is negative, while that gyrating inside is positive. For example, in case the electron number density increases outward, the negative contribution to v_θ may exceed the positive one locally because v_θ is weighted by the electron population as defined in Eq. (4).

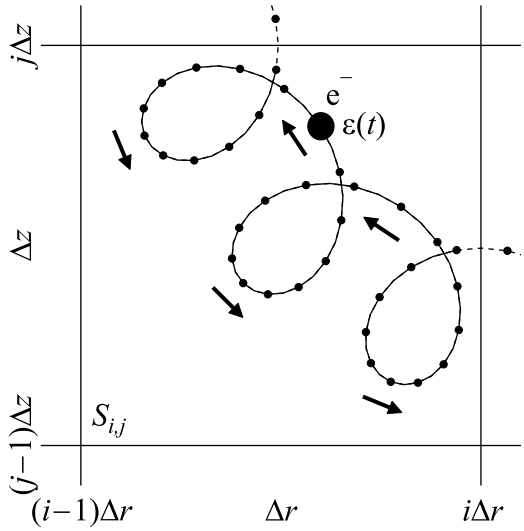

Fig. 5. Schematic of sampling for EEG in a sampling section $S_{i,j}$. The EEG was sampled as the average of $\Delta\varepsilon/\Delta t$ for the electrons flying in $S_{i,j}$. The energies brought by an electron into or out of $S_{i,j}$ are not sampled.

3.3 Electron energy gain

The EEG G is defined as the energy gained by an electron per unit time in a sampling section (see Fig. 5). The quantity of the EEG is represented by introducing "the EEG unit" to denote eV(RF period)$^{-1}$(electron)$^{-1}$ in this paper; 1 eV(RF period)$^{-1}$(electron)$^{-1}$ $= e \times (1\,\mathrm{V})/T_{\mathrm{RF}} = 2.17 \times 10^{-12}$ W/electron. If the electron number density n is given as a function of the position, the instantaneous plasma power would be obtained by integrating G with the weight of n over the space in the chamber.

The sampling for the EEG was done as follows:

$$G(S_{i,j},t) = \left(\sum_{S_{i,j}\ni \boldsymbol{r}_k} \Delta\varepsilon_k(t)/\Delta t\right) / \left(\sum_{S_{i,j}\ni \boldsymbol{r}_k} 1\right), \tag{7}$$

$$\Delta\varepsilon_k(t) = \varepsilon_k(t) - \varepsilon_k(t-\Delta t), \tag{8}$$

where

$$\varepsilon_k(t) = \frac{1}{2}m\left\{[v_{x,k}(t)]^2 + [v_{y,k}(t)]^2 + [v_{z,k}(t)]^2\right\}. \tag{9}$$

The energies brought by an electron into or out of $S_{i,j}$ are not sampled in order to evaluate only the energy increase or decrease during the flight in $S_{i,j}$; otherwise, G becomes unfavorably zero for an electron which passes through $S_{i,j}$ collisionless even though it may obtain energy during its stay in $S_{i,j}$. The electron energy loss by the collisions was sampled separately.

The EEG was represented in the following form:

$$\begin{aligned} G(S_{i,j},t) &= G_2(S_{i,j})\sin[2\omega_{\mathrm{RF}}t-\gamma_2(S_{i,j})] \\ &\quad + G_1(S_{i,j})\sin[\omega_{\mathrm{RF}}t-\gamma_1(S_{i,j})] \\ &\quad + G_0(S_{i,j}). \end{aligned} \tag{10}$$

The first term in the right-hand side represents that the EEG may take peaks twice in an RF period corresponding to the positive and negative peaks of $E_\theta(t)$. G_2 represents the amplitude of the EEG, which is a sensitivity of the electron response. G_2 was taken to be positive to make the fitting function unique, and its phase delay γ_2 is defined in a range of $-\pi \le \gamma_2 < \pi$ along the relationship between the fitting parameters derived in Sect. 3.4. G_1 represents a distortion of the EEG profile due to a kind of directionality of the electron flow as quantified above with v_0. G_1 may potentially be a measure to evaluate how far the impedance matching between the plasma and the external circuit can be achieved. G_1 may have both positive and negative values; e.g. $G_1 < 0$ in case the $G(t)$ is larger in the latter half of an RF period than in the former half. Its phase delay γ_1 was defined to satisfy $-\pi/2 \le \gamma_1 \le \pi/2$. G_0 is the time-averaged EEG. The plasma power in a static picture would be estimated by integrating nG_0 of all $S_{i,j}$.

3.4 Relation between fitting parameters

The EEG $G(t)$ is equivalent to power per electron. $G(t)$ is represented as the product between the Coulomb force $F(t)$ acting on an electron and $v_\theta(t)$ along the induced electric field $E_\theta(t)$:

$$F(t) = -eE_\theta(t), \tag{11}$$

$$E_\theta(t) = -E_{\max}\sin\omega_{\mathrm{RF}}t, \tag{12}$$

$$G(t) = v_\theta(t)F(t) = v_\theta(t)eE_{\max}\sin\omega_{\mathrm{RF}}t. \tag{13}$$

By substituting Eq. (6) for $v_\theta(t)$ in Eq. (13), G is obtained as

$$\begin{aligned} G(t) &= \frac{1}{2}v_1eE_{\max}\sin\left[2\omega_{\mathrm{RF}}t-\left(\phi_1+\frac{\pi}{2}\right)\right] \\ &\quad + v_0eE_{\max}\sin\omega_{\mathrm{RF}}t+\frac{1}{2}v_1eE_{\max}\cos\phi_1. \end{aligned} \tag{14}$$

By comparing this expression with Eq. (10), the fitting parameters are related as follows:

$$G_2 = \frac{1}{2}v_1eE_{\max}, \tag{15}$$

$$\gamma_2 = \phi_1+\frac{\pi}{2}, \tag{16}$$

$$G_1 = v_0eE_{\max}, \tag{17}$$

$$\gamma_1 = 0, \tag{18}$$

Table I. Evaluation of the fitting precision. The effective number of sampled electrons, $n_{\rm smp}$, and the rms deviations σ_G and $\sigma_{v\theta}$ of $G(t)$ and $v_\theta(t)$ between the sampled data and the re-composed curves relative to $\max(|G(t)|)$ and $\max(|v_\theta(t)|)$, respectively.

Sampling sections; regions	Fig.	$n_{\rm smp}$	σ_G	$\sigma_{v\theta}$
$S_{28,80}$; near-antenna	8(b)	$> 7.6 \times 10^6$	4.0%	4.8%
$S_{40,73}$; near-sidewall	8(c)	$> 4.9 \times 10^7$	2.5%	3.8%
$S_{4,48}$; RF-resonant	8(d)	$> 2.0 \times 10^5$	10.3%	8.4%
$S_{40,80}$; outermost near-ceiling	9(b)	$> 1.4 \times 10^7$	5.4%	7.9%
$S_{38,80}$; outer near-ceiling	9(c)	$> 5.6 \times 10^7$	7.6%	22.1%

$$G_0 = \frac{1}{2} v_1 e E_{\max} \cos\phi_1. \tag{19}$$

These relations indicate dependence of the waveform of $G(t)$ on macroscopic quantities. The sensitivity factors G_2 and v_1 in Eq. (15), which represent the electron response to the RF electric field, are proportional. The distortion factor G_1 in Eq. (17) is directly dependent on the directionality factor v_0. The time-averaged EEG G_0 in Eq. (19), which represents net power deposition at a position, has three factors of the sensitivity v_1, the amplitude $E_{\max}$, and the power factor $\cos\phi_1$.

4. Results and discussion

The position dependence of the fitting parameters G_2, γ_2, G_1, γ_1, and G_0 for $G(t)$, and v_1, ϕ_1, and v_0 for $v_\theta(t)$ is shown in Figs. 6 and 7. G_0 in Fig. 6(c) shows the three primary regions of high EEG. The EEG profiles in these regions are detailed afterward in the following sections. The fitting results include large fluctuations in the lower region and around the central axis, where the number of sampled electrons, $n_{\rm smp}$, is small. The re-composed time-resolved profiles of $G(t)$ and $v_\theta(t)$ at specific positions focused on afterward are shown in Figs. 8 and 9. $n_{\rm smp}$ of the data used for the curve fitting of $G(t)$ and $v_\theta(t)$ in Figs. 8 and 9 is shown in Table I together with the rms deviations σ_G and $\sigma_{v\theta}$ between the data and the re-composed curves of $G(t)$ and $v_\theta(t)$ as relative values to $\max(|G(t)|)$ and $\max(|v_\theta(t)|)$, respectively. The rms deviations higher than 10% are of the cases in which $n_{\rm smp}$ is small or the absolute value of the fitted quantity is small. However, the fitting has successfully reproduced primary profiles of $G(t)$ and $v_\theta(t)$. This indicates that the assumption on the fitting functions were appropriate. As well, γ_2 in Fig. 6(d) and ϕ_1 in Fig. 7(c) seem to satisfy the relationship in Eq. (16) widely in the upper region and $\gamma_1 \approx 0$ in most regions as predicted in Eq. (18), which supports the validity of the relationship between the fitting parameters in Eqs. (15)–(19).

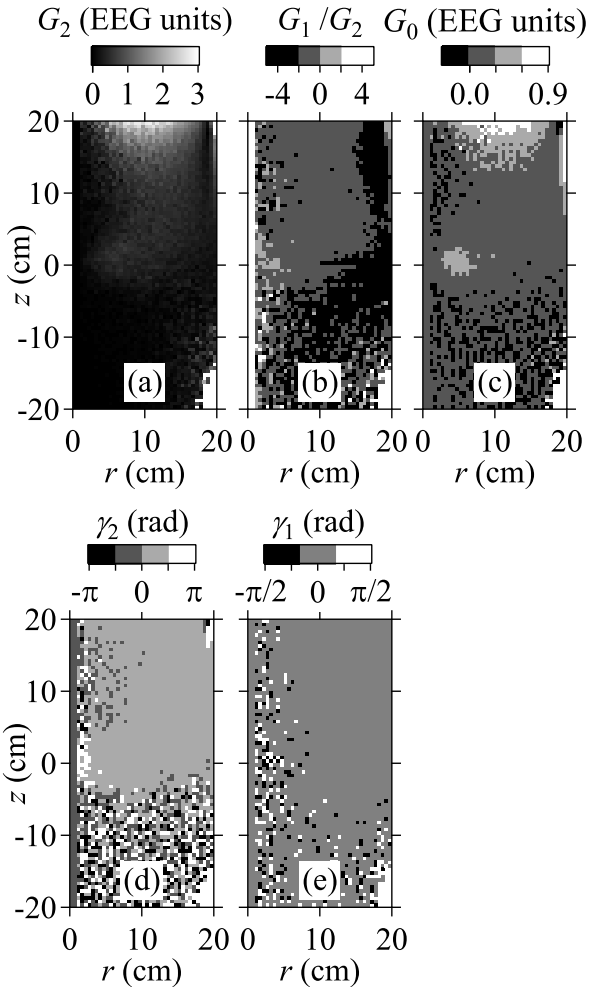

Fig. 6. Spatial distribution of fitting parameters: (a) G_2, the amplitude of the EEG; (b) G_1/G_2, the degree of asymmetry of the EEG between the former and latter halves of an RF period; (c) G_0, the time-averaged EEG in an RF period; (d) γ_2, the phase shift of the component of $\sin 2\omega_{\mathrm{RF}}t$ of the EEG; and (e) γ_2, the phase shift of the component of $\sin \omega_{\mathrm{RF}}t$ of the EEG. The EEG units represent eV(RF period)$^{-1}$(electron)$^{-1}$.

4.1 Profiles in near-antenna region

This region locates in the vicinity of the RF antenna. Because $E_{\max}$ is large here, it is considered that the plasma is mainly sustained by the power given in this region.

G_2 and G_0 in Figs. 6(a) and 6(c), respectively, were large in this region correspondingly to large $E_{\max}$. The tendency of their intensity decay with the distance from the antenna is similar to that of $E_{\max}$ in Fig. 2(a). γ_2 took small positive values, that represents slight delays of $G(t)$ from $E_\theta(t)$. The ratio G_1/G_2 in Fig. 6(b), that represents the asymmetry of the EEG between the former and latter halves of an RF period, was negative; i.e. the negative EEG is enhanced in the former half of an RF period, and the positive EEG becomes large in the latter. These profiles of γ_2 and G_1/G_2 apply to a wide area in the chamber.

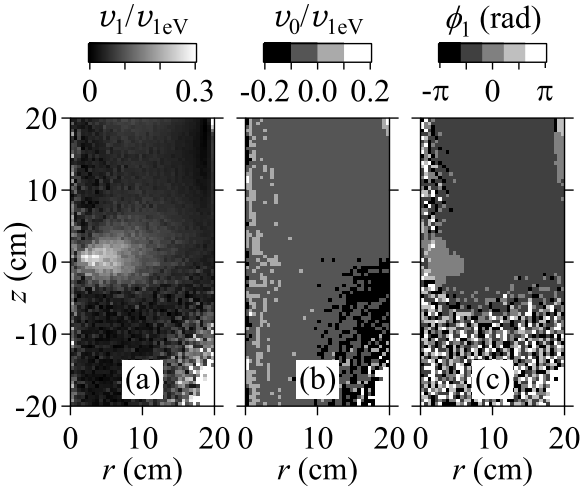

Fig. 7. Spatial distribution of fitting parameters: (a) v_1/v_{1eV}, the amplitude of v_θ normalized by v_{1eV}; (b) v_0/v_{1eV}, the time-averaged v_θ normalized by v_{1eV} representing the directionality of the azimuthal electron flow; and (c) ϕ_1, the phase shift of the component of $\sin\omega_{RF}t$ of v_θ.

On $v_\theta(t)$, v_0 in Fig. 7(b) shows negative values, i.e. the time-averaged azimuthal electron flow is directional, and clockwise relative to the z-axis. This directionality agrees with that of the grad-$\boldsymbol{B}$ drift. ϕ_1 in Fig. 7(c) was around $-\pi/2$, that represents the phase of $v_\theta(t)$ leads that of $E_\theta(t)$. These profiles are also common in a wide area in the chamber.

The influence of the chamber ceiling as a boundary did not appear significantly. This is because the electron reflection at the chamber ceiling, which the magnetic flux lines reach almost vertically, does not disturb the cyclotron motion itself.

4.2 Profiles in the near-sidewall region

In this region, the magnetic field lines run with shallow angles relative to the sidewall. The shallower the angle of the magnetic field lines is, the more the electron reflection likely to succeed, that may enhance the directional electron flow. It was pointed out that the EEG mechanism is strongly dependent on the angle of the magnetic field lines incident on the wall.[43] Here, the $G(t)$ and $v_\theta(t)$ profiles around $S_{40,80}$, in which the magnetic field lines run almost in parallel to the sidewall, are mentioned separately in Sect. 4.4.

G_0 is large and $G_1 < 0$ in this region [Figs. 6(b) and 6(c)]. These are the same as is in the near-antenna region. A difference is that γ_2 is close to $+\pi/2$ [Fig. 6(d)]. $v_0 < 0$, and v_1 does not vary significantly from the near-antenna region [Figs. 7(a) and 7(b)]. ϕ_1 took small negative values around zero [Fig. 7 (c)].

The reason why G_0 was large although v_1 and E_{max} are not significant here is that $v_\theta(t)$ is almost synchronous to $E_\theta(t)$. Thus, the power factor $\cos\phi_1$ is high (≈ 1) in this region, which represents that the electron acceleration succeeds long. It is considered that the electron reflec-

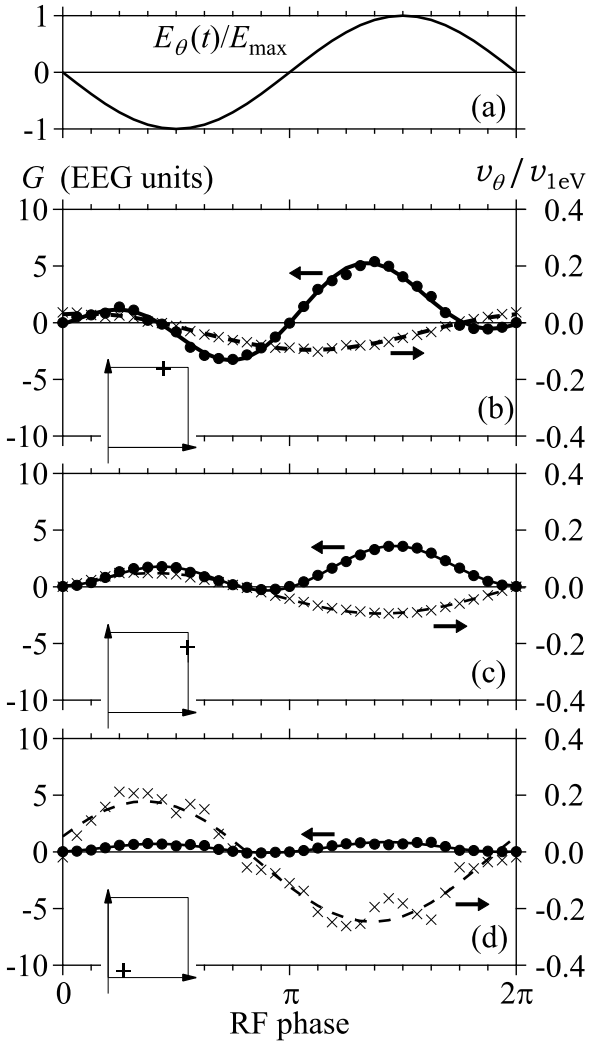

Fig. 8. Phase-resolved profile of the EEG $G(t)$ (•, sampled; and solid curves, fitting) and the $v_\theta(t)$ normalized by $v_{1\mathrm{eV}}$ (×, sampled; and broken curves, fitting) in some sampling sections $S_{i,j}$. (a) waveform of the induced electric field; (b) $S_{28,80}$ near the chamber ceiling; (c) $S_{40,73}$ beside the sidewall far from the chamber ceiling; and (d) $S_{4,48}$ around the RF-resonant region. The EEG units represent eV(RF period)$^{-1}$(electron)$^{-1}$. $v_{1\mathrm{eV}}$ is the electron speed associated with 1 eV.

tion at the sidewall contributes to large G_0 via high power factor. This tendency is observed widely along the sidewall in the upper region. However, its intensity decreases downward to the separatrix, where the magnetic field lines are incident to the sidewall vertically.

It is considered that the EEG mechanism in this region would be significant when the ICP is driven by an antenna placed around the sidewall of the cylindrical chamber as seen in the neutral loop discharge plasmas.[25,26,54]

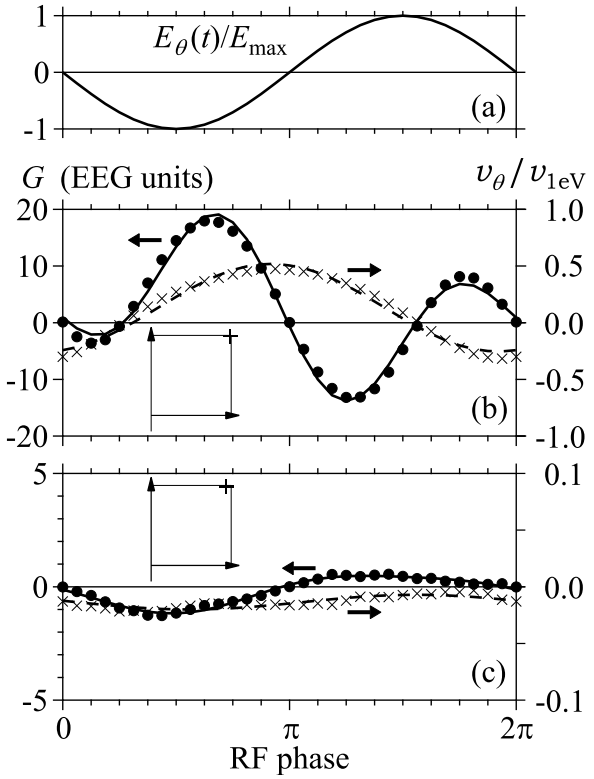

Fig. 9. Phase-resolved profile of the EEG $G(t)$ (•, sampled; and solid curves, fitting) and the $v_\theta(t)$ normalized by $v_{1\mathrm{eV}}$ (×, sampled; and broken curves, fitting) in some sampling sections $S_{i,j}$. (a) waveform of the induced electric field; (b) $S_{40,80}$ beside the sidewall near the chamber ceiling; (c) $S_{38,80}$ around the intermediate region between the near-ceiling and near-sidewall regions. The EEG units represent eV(RF period)$^{-1}$(electron)$^{-1}$. $v_{1\mathrm{eV}}$ is the electron speed associated with 1 eV.

4.3 Profiles around the RF-resonant region

The ECR occurs temporarily in the RF-resonant region, where $|\boldsymbol{B}| = B_{\mathrm{ECR}} = 2\pi(m/e)f_{\mathrm{RF}} = 0.48\,\mathrm{mT}$ at $f_{\mathrm{RF}} = 13.56\,\mathrm{MHz}$. However, this EEG mechanism does not continue long because the accelerated electrons easily escape from this region.[27]

In this region, G_0 is locally larger than in its circumambient region [Fig. 6(c)], and $G_1 < 0$ and γ_2 close to $+\pi/2$ are the same as in the near-sidewall region [Figs. 6(b) and (d)]. Negative v_0 and small negative ϕ_1 values are also similar to those in the near-sidewall region, but it is characteristic that v_1 is large (Fig. 7), i.e. electron motion responded to the alternation of $E_\theta(t)$ intensely, and $v_\theta(t)$ is always oriented to the direction of the acceleration due to $E_\theta(t)$ (Fig. 8).

In the RF-resonant region, $E_{\max}$ is small for a long distance from the antenna, but large v_1 and high power factor $\cos\phi_1 \approx 1$ resulted in large G_0 values. The phase at which electrons enter this region is random, thus both energy gain and loss may occur. However, the energy gain exceeded the loss stochastically, that caused the large G_0 values. The EEG in the RF-

resonant region seems to be a collisionless heating unlike that in the near-antenna region to compensate or balance the energy loss by inelastic collisions. Additional simulations at lower pressures showed that the EEG in the RF-resonant region and the near-sidewall region was kept high while that in the near-antenna region decreased. When the magnetic field is designed so that the RF-resonant region is close to the RF antenna, the resonance-based EEG mechanism may have a primary role in supplying energy to electrons.

4.4 Other profiles

Unlike the profiles in the three primary regions mentioned above, particular tendencies were observed around the border region between the near-antenna and near-sidewall regions. The re-composed time-resolved profiles of $G(t)$ and $v_\theta(t)$ in this region are shown in Fig. 9. Two aspects are pointed out here.

Firstly, around $S_{40,80}$ at the corner, where the chamber ceiling and sidewall meet and the electron number density $n(r,z)$ is high, $G_1 > 0$ and $v_0 > 0$, which are different from the three regions [Figs. 6(b) and 7(b)]. Furthermore, v_1 is the largest here over the chamber space [Fig. 7(a)], and resultingly, G_0 represented by v_1 as Eq. (19) is also the largest [Fig. 6(c)].

Secondly, around $S_{38,80}$ on the border between the near-antenna and near-sidewall regions, the power factor $\cos\phi_1 < 0$ and thus $G_0 < 0$ [Figs. 7(c) and 6(c)]. From Eq. (19), the sign of G_0 is determined by that of the power factor $\cos\phi_1$. This seems similar to experimental results on negative power absorption.[35,37,38] In addition, $v_\theta(t)$ is always negative in $S_{38,80}$. $v_\theta(t)$ is dependent on the gradient of $n(r,z)$ in the radial direction as mentioned in Sect. 3.2.

In the present simulation condition, $n(r, Z_{\mathrm{top}})$ near the chamber ceiling had its peak midway between the central axis and the sidewall. This peak moved outward and inward in an RF period, and its time-averaged position was around $S_{38,80}$. This resulted in $v_0 > 0$ in $S_{40,80}$ at the corner while $v_0 < 0$ inside the $n(r, Z_{\mathrm{top}})$ peak in the vicinity of the RF antenna, through the relationship between $n(r,z)$ and $v_\theta(t)$ mentioned in Sect. 3.2. Here, this specific peak position, denoted by $i = 38$ above, may change depending on the conditions for the plasma operation. However, it is probable that a peak of $n(r, Z_{\mathrm{top}})$ appear somewhere between $r = 0$ and 20 cm because the peak of $E_{\max}$ appears around $r = 14$ cm (Fig. 2) This is also indicated by an observation of optical emission from a H_2 X-point plasma.[18] It is inferred that there is a relationship between the passage of the $n(r,z)$ peak and the negative G_0. The reason why $G_0 < 0$ at the $n(r, Z_{\mathrm{top}})$ peak position is left for further investigation.

5. Conclusions

Time-resolved analyses on the electron energy gain (EEG) $G(t)$ and the azimuthal electron velocity $v_\theta(t)$ were performed using a Monte Carlo method in order to characterize the region-dependent electron energy deposition in an inductively coupled RF plasma driven under confronting divergent magnetic fields. $G(t)$ and $v_\theta(t)$ were successfully fitted by functions

consisting of constant and sinusoidal terms up to the second-order harmonic for $G(t)$ and up to the first-order one for $v_\theta(t)$.

It was derived theoretically that G_0 is dependent on the amplitude v_1 of $v_\theta(t)$, the power factor $\cos\phi_1$ determined by the phase difference ϕ_1 between the electric field and $v_\theta(t)$, and the amplitude of the electric field $E_{\max}$, from the relationship between $G(t)$ and $v_\theta(t)$ using the fitting parameters to express $G(t)$ and $v_\theta(t)$. The time-averaged power deposition G_0 is particularly important for plasma sustainment. We examined the mechanism of the EEG in three primary high-EEG regions and other characteristic regions.

In the near-antenna region where the $E_{\max}$ is large, we observed an asymmetric EEG that the EEG is large in the latter half of an RF period. The time-averaged azimuthal electron flow was biased toward the clockwise direction. These profiles were common widely in the chamber. G_0 in this region was enhanced by the large $E_{\max}$.

In the near-sidewall region, where magnetic field lines run with shallow angles relative to the sidewall, the power factor was high as $\cos\phi_1 \approx 1$ and G_0 was also high. This tendency is considered to be influenced by reflection at the sidewall that assists continuous electron acceleration along the sidewall via inducing a directional electron drift.

Around the RF-resonant region, where the partial resonance occurs, G_0 was high. This was due to large v_1 and high power factor $\cos\phi_1 \approx 1$.

In addition, some particular profiles were observed locally near the corner at which the chamber ceiling and sidewall meet. $G(t)$ was asymmetrically large there in the former half of an RF period and $v_\theta(t)$ was biased toward the counterclockwise direction unlike in the three primary regions. It was considered that the high G_0 was due to the largest v_1 over the chamber. It is known that the asymmetry of $v_\theta(t)$ is induced by the electron number density gradient $\partial n(r,z)/\partial r$, which increases outward, takes its peak midway, and decreases toward the sidewall typically. Furthermore, G_0 was negative around the peak of $n(r,z)$. Further investigation is necessary to clarify the reasons of the large v_1 and negative G_0 around this region.

Experimental measurement on the directionality of $v_\theta(t)$ is expected to relate the asymmetry in $v_\theta(t)$ with $\partial n(r,z)/\partial r$. This is an interesting physics to be clarified. Nonetheless, the present findings on the EEG mechanisms, which are dependent on the positions characterized by the geometries of the reactor and the $\boldsymbol{E}$ and $\boldsymbol{B}$ fields, would be informative for efficient EEG in the design of advanced magnetized ICP reactors for new functional applications.

Acknowledgments

This work was supported by KAKENHI Grants JP16K05626 and JP19K03780 from the Japan Society for the Promotion of Science.

References

1) M. M. M. Bilek, J. Appl. Phys. **85**, 6385 (1999).
2) M. M. M. Bilek and I. G. Brown, IEEE Trans. Plasma Sci. **27**, 193 (1999).
3) B. K. Tay, G. F. You, S. P. Lau, and X. Shi, Surf. Coat. Technol. **133-134**, 593 (2000).
4) T. Zhang, D. T. K. Kwok, P. K. Chu, and I. G. Brown, J. Appl. Phys. **89**, 672 (2001).
5) A. Anders, IEEE Trans. Plasma Sci. **30**, 108 (2002).
6) E. Byon and A. Anders, J. Appl. Phys. **93**, 8890 (2003).
7) E. Byon, J.-K. Kim, S.-C. Kwon, and A. Anders, IEEE Trans. Plasma Sci. **32**, 433 (2004).
8) Y. Hu, L. Li, M. Xu, Y. Liu, X. Cai, I. G. Brown, and P. K. Chu, Rev. Sci. Instrum. **76**, 023303 (2005).
9) H. Sugawara and S. Ogino, Jpn. J. Appl. Phys. **55**, 07LD05 (2016).
10) O. Fukumasa, Y. Tauchi, and S. Sakiyama, Jpn. J. Appl. Phys. **36**, 4593 (1997).
11) N. Hayashi, T. Nakashima, and H. Fujita, Jpn. J. Appl. Phys. **38**, 4301 (1999).
12) T. A. Santhosh Kumar, S. K. Mattoo, and R. Jha, Phys. Plasmas **11**, 1735 (2004).
13) St. Kolev, St. Lishev, A. Shivarova, Kh. Tarnev, and R. Wilhelm, Plasma Phys. Control. Fusion **49**, 1349 (2007).
14) A. Aanesland, J. Bredin, P. Chabert, and V. Godyak, Appl. Phys. Lett. **100**, 044102 (2012).
15) G. Fubiani and J. P. Boeuf, Plasma Sources Sci. Technol. **24**, 055001 (2015).
16) J. Y. Kim, W.-H. Cho, J.-J. Dang, and S. Kim, Plasma Sources Sci. Technol. **25**, 065019 (2016).
17) Y. Celik, T. Tsankov, and U. Czarnetzki, IEEE Trans. Plasma Sci. **39**, 2466 (2011).
18) T. Tsankov and U. Czarnetzki, IEEE Trans. Plasma Sci. **39**, 2538 (2011).
19) T. Tsankov and U. Czarnetzki, AIP Conf. Proc. **1390**, 140 (2011).
20) T. V. Tsankov, K. Toko, and U. Czarnetzki, Phys. Plasmas **19**, 123503 (2012).
21) K. Nakashima and H. Sugawara, Technical Meet. Plasma and Pulsed Power, IEE Japan, 2018, PPP-18-037 [in Japanese].
22) H. Sugawara, K. Nakashima, and H. Takahashi, Proc. 20th Gaseous Electronics Meet., 2018, B-1.
23) H. Sugawara, K. Nakashima, and H. Takahashi, Proc. 24th Europhysics Conf. Atomic and Molecular Physics of Ionized Gases, 2018, P-112.
24) H. Takahashi, K. Nakashima, T. Yamamoto, and H. Sugawara, Jpn. J. Appl. Phys. **57**, 126101 (2018).

25) T. Uchida, J. Vac. Sci. Technol. A **16**, 1529 (1998).

26) T. Uchida and S. Hamaguchi, J. Phys. D **41**, 083001 (2008).

27) Y. Minami, Y. Asami, and H. Sugawara, IEEE Trans. Plasma Sci. **42**, 2550 (2014).

28) K. Kondo, H. Kuroda, and T. Makabe, Jpn. J. Appl. Phys. **33**, 4254 (1994).

29) A. Okigawa, T. Makabe, T. Shibagaki, N. Nakano, Z. Lj. Petrović, T. Kogawa, and A. Itoh, Jpn. J. Appl. Phys. **35**, 1890 (1996).

30) M. Tadokoro, H. Hirata, N. Nakano, Z. Lj. Petrović, and T. Makabe, Phys. Rev. E, **57**, R43 (1998).

31) M. Tadokoro, H. Hirata, N. Nakano, Z. Lj. Petrović, and T. Makabe, Phys. Rev. E, **58**, 7823 (1998).

32) K. Kamimura, K. Iyanagi, N. Nakano, and T. Makabe, Jpn. J. Appl. Phys. **38**, 4429 (1999).

33) M. M. Turner, Phys. Rev. Lett. **71**, 1884 (1993).

34) V. I. Kolobov and D. J. Economou, Plasma Sources Sci. Technol. **6**, R1 (1997).

35) V. A. Godyak, Phys. Rev. Lett. **79**, 4589 (1997).

36) V. A. Godyak, R. B. Piejak, B. M. Alexandrovich, and V. I. Kolobov, Phys. Rev. Lett. **80**, 3264 (1998)

37) Z. F. Ding, B. Sun, and W. G. Huo, Phys. Plasma **22**, 063504 (2015).

38) Z. F. Ding, B. Sun, and W. G. Huo, Phys. Plasma **22**, 089901 (2015).

39) A. V. Arsenin, V. G. Leiman, and V. P. Tarakanov, J. Plasma Fusion Res. Series **8**, 1622 (2009) (Proc. 14th Int. Congress Plasma Phys., 2008).

40) Y. Asami and H. Sugawara, IEEE Trans. Plasma Sci. **42**, 2540 (2014).

41) H. Takahashi and H. Sugawara, Proc. 2018 Annual Conf. Fundamentals and Materials Soc. JEE Japan, 2018, 4-A-a1-1 [in Japanese].

42) H. Takahashi and H. Sugawara, 2019 National Convention IEE Japan, 2019, 1-066 [in Japanese].

43) H. Takahashi and H. Sugawara, Proc. XXXIV Int. Conf. Phenomena in Ionized Gases and 10th Int. Conf. Reactive Plasmas, 2019, PO18AM-004.

44) R. Ozawa and H. Sugawara, 2019 National Convention IEE Japan, 2019, 1-065 [in Japanese].

45) H. Sugawara, N. Mori, Y. Sakai, and Y. Suda, J. Comput. Phys. **223**, 298 (2007).

46) Y. Nakamura and M. Kurachi, J. Phys. D **21**, 718 (1988).

47) H. Tsuboi and S. Ogata, Jpn. J. Appl. Phys. **46**, 7475 (2007).

48) D. O'Connell, T. Gans, D. L. Crintea, U. Czarnetzki, and N. Sadeghi Plasma Sources Sci. Technol. **17**, 024022 (2008).

49) H. Sugawara and Y. Sakai, J. Phys. D **41**, 135208 (2008).

50) T. Osaga and H. Sugawara, Plasma Sources Sci. Technol. **20**, 065003 (2011).

51) H. Sugawara, T. Osaga, and H. Yamamoto, Plasma Sources Sci. Technol. **20**, 055002 (2011).

52) Z. Yoshida and T. Uchida, Jpn. J. Appl. Phys. **34**, 4213 (1995).

53) Z. Yoshida, H. Asakura, H. Kakuno, J. Morikawa, K. Takemura, S. Takizawa, and T. Uchida, Phys. Rev. Lett. **81**, 2458 (1998).

54) T. Uchida, Jpn. J. Appl. Phys. **33**, L43 (1994).